

Robust charge-density wave correlations in the electron-doped single-band Hubbard model

Peizhi Mai,^{1,2} Nathan S. Nichols,³ Seher Karakuzu,^{1,4} Feng Bao,⁵
Adrian Del Maestro,^{6,7,8} Thomas A. Maier,¹ and Steven Johnston^{6,7}

¹*Computational Sciences and Engineering Division, Oak Ridge National Laboratory, Oak Ridge, Tennessee, 37831-6494, USA*

²*Department of Physics and Institute of Condensed Matter Theory,
University of Illinois at Urbana-Champaign, Urbana, Illinois 61801, USA*

³*Data Science and Learning Division, Argonne National Laboratory, Argonne, Illinois 60439, USA*

⁴*Center for Computational Quantum Physics, Flatiron Institute, 162 5th Avenue, New York, New York 10010, USA*

⁵*Department of Mathematics, Florida State University, Tallahassee, Florida 32306, USA*

⁶*Department of Physics and Astronomy, The University of Tennessee, Knoxville, Tennessee 37996, USA*

⁷*Institute of Advanced Materials and Manufacturing, The University of Tennessee, Knoxville, Tennessee 37996, USA*

⁸*Min H. Kao Department of Electrical Engineering and Computer Science,
University of Tennessee, Knoxville, Tennessee 37996, USA*

(Dated: October 28, 2022)

There is growing evidence that the hole-doped single-band Hubbard and t - J models do not have a superconducting ground state reflective of the high-temperature cuprate superconductors but instead have striped spin- and charge-ordered ground states. Nevertheless, it is proposed that these models may still provide an effective low-energy model for electron-doped materials. Here we study the finite temperature spin and charge correlations in the electron-doped Hubbard model using quantum Monte Carlo dynamical cluster approximation calculations and contrast their behavior with those found on the hole-doped side of the phase diagram. We find evidence for a charge modulation with both checkerboard and unidirectional components decoupled from any spin-density modulations. These correlations are inconsistent with a weak-coupling description based on Fermi surface nesting, and their doping dependence agrees qualitatively with resonant inelastic x-ray scattering measurements. Our results provide evidence that the single-band Hubbard model describes the electron-doped cuprates.

A key question in quantum materials research is whether or not the single-band Hubbard model describes the properties of the high-temperature (high- T_c) superconducting cuprates [1–3]. On the one hand, several studies have demonstrated a direct mapping between multi-orbital Cu-O models and effective single-band descriptions [4–7]. At the same time, quantum cluster methods have found evidence for a d -wave superconducting state [6, 8] in the Hubbard model, with a nonmonotonic T_c as a function of doping that resembles the dome found in real materials. On the other hand, a growing number of state-of-the-art numerical studies on extended Hubbard and t - J clusters have found evidence for stripe-ordered ground states for model parameters relevant to the cuprates [9–13]. While density matrix renormalization group (DMRG) simulations of multi-leg hole (h)-doped Hubbard ladders do obtain a superconducting ground state for nonzero values of the next-nearest-neighbor hopping t' [14], its order parameter does not have the correct $d_{x^2-y^2}$ symmetry [15] found in the cuprates [16]. Conversely, DMRG calculations for six- and eight-leg t - J cylinders obtain the correct order parameter but only on the electron (e)-doped side of the phase diagram [12]. These results cast significant doubt on the long-held belief that the Hubbard model describes the h -doped cuprates. Nevertheless, hope remains that it may capture the e -doped materials.

From an experimental perspective, charge-density-wave (CDW) correlations have been established as a

ubiquitous feature of the underdoped cuprates [17, 18]. Initially observed by inelastic neutron scattering in the form of intertwined spin and charge stripes [19], short-range CDW correlations have now been reported in nearly all families of cuprates using scanning tunneling microscopy [20, 21] and resonant inelastic x-ray scattering (RIXS) [22–33]. Importantly, these CDW correlations persist up to high temperatures, particularly on the e -doped side of the phase diagram [25, 28–30].

Given their ubiquity, these CDW correlations must be accounted for by any proposed effective model for the cuprates. Evidence for charge modulations, both in the form of unidirectional stripe correlations or short-range CDW correlations, has now been found in a variety of finite temperature quantum Monte Carlo (QMC) simulations of the h -doped Hubbard model [13, 34–38]. These simulations are generally restricted to high temperatures by the Fermion sign problem [10, 34, 35] (except for very recent constrained path QMC calculations [38]) and focus on the h -doped model. The observed cuprate CDWs exhibit a significant electron-hole asymmetry, however. On the h -doped side, they can intertwine with spin-density modulations to form stripes while they coexist with uniform antiferromagnetic (AFM) correlations on the e -doped side [25, 28, 30]. These differences have raised questions on whether the e - and h -doped CDWs share a common origin [29, 30].

Here, we study and contrast the spin and charge correlations of the two-dimensional Hubbard model

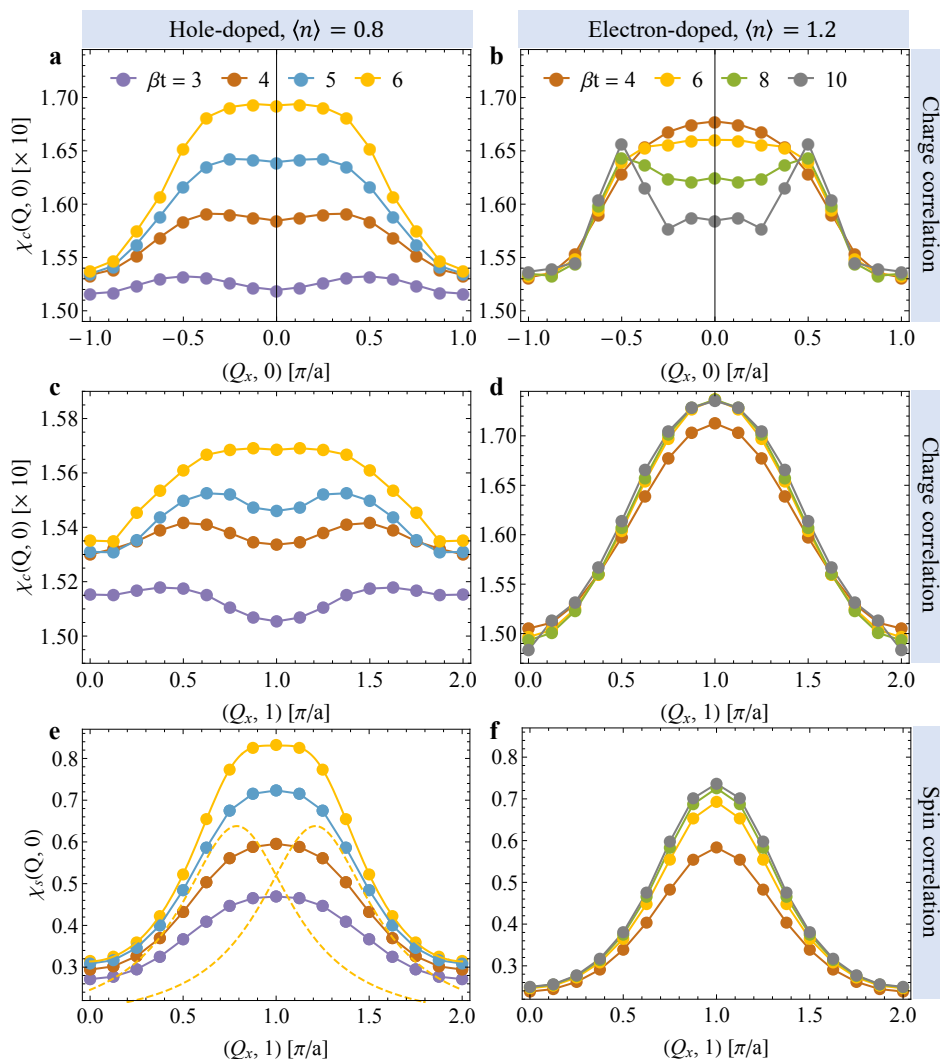


FIG. 1. **Static spin and charge correlations in the doped single-band Hubbard model.** Panels a and c show the static charge susceptibility $\chi_c(\mathbf{Q}, 0)$ along the $(Q_x, 0)$ and $(Q_x, \pi/a)$ directions, respectively, for the hole-doped system with $t'/t = -0.2$ and $\langle n \rangle = 0.8$. Panel e shows the corresponding static spin susceptibility $\chi_s(\mathbf{Q}, 0)$ along the $\mathbf{Q} = (Q_x, \pi/a)$ direction. The yellow dashed lines show incommensurate peaks obtained from fitting multiple Lorentzian functions plus a constant background to the $\beta t = 6$ data. (The constant contribution is not shown.) Panels b, d, f show the corresponding results for the e -doped case with $t'/t = -0.2$ and $\langle n \rangle = 1.2$. These results were obtained using a 16×4 cluster, and the inverse temperatures $\beta = 1/T$ are reported in units of $1/t$.

using the dynamical cluster approximation (DCA) [39] and a nonperturbative QMC cluster solver [40] (see methods). Working on large (16×4) rectangular clusters that are wide enough to support large-period stripe correlations if they are present [34], we vary the electron density $\langle n \rangle$ across both sides of the phase diagram to contrast the correlations in each case. Our calculations uncover robust two-component CDW correlations on the e -doped side, which consists of superimposed checkerboard $(\pi/a, \pi/a)$ and unidirectional $\mathbf{Q}_{\text{CDW}} = (\pm\delta_c, 0)$ components. These CDW correlations appear to be decoupled from any stripe-like modulations of the spins and instead coexist with short-range antiferromagnetic correlations. This behavior is in direct contrast to the

h -doped case, where we find evidence for fluctuating stripe correlations in both the charge and spin degrees of freedom [34]. Our results agree with experimental observations on the e -doped cuprates, including the observed doping dependence of \mathbf{Q}_{CDW} . This supports the notion that the single-band Hubbard model captures the e -doped side of the high- T_c phase diagram.

Results. Figure 1 compares the static charge $\chi_c(\mathbf{Q}, \omega = 0)$ and spin $\chi_s(\mathbf{Q}, 0)$ susceptibilities for the h - ($\langle n \rangle = 0.8$) and e -doped ($\langle n \rangle = 1.2$) Hubbard model with $U/t = 6$, $t'/t = -0.2$, and varying temperature. In the h -doped case (Fig. 1a,c,e), unidirectional charge and spin stripes form as the temperature is lowered, consistent with prior

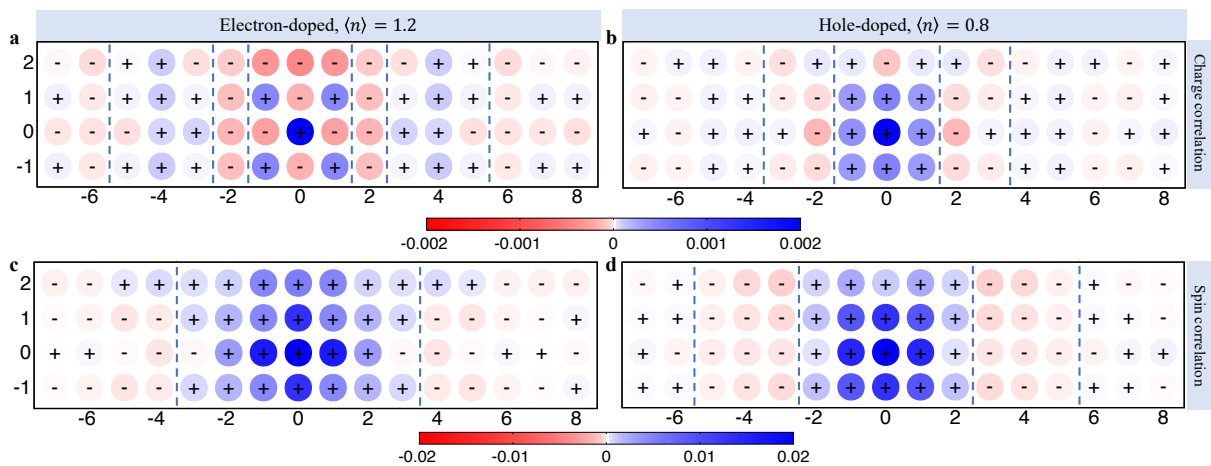


FIG. 2. **Static spin and charge correlations in real-space.** **a** $\chi_c(\mathbf{r}, 0)$ for the electron-doped system ($t' = -0.2t$, $\langle n \rangle = 1.2$) at the lowest accessible inverse temperature $\beta t = 10$. **b** $\chi_c(\mathbf{r}, 0)$ for the h -doped system ($t' = -0.2t$, $\langle n \rangle = 0.8$) at the lowest accessible inverse temperature $\beta t = 6$. **c** and **d** show the staggered spin-spin correlations $\chi_{s,\text{stag}}(\mathbf{r}, 0)$ for the h - and e -doped cases, respectively. The dashed lines indicate the approximate nodes in the spin and charge stripe modulations.

finite-temperature studies [34, 35, 38]. These correlations manifest as incommensurate peaks in the static susceptibility at wave vectors $\mathbf{Q}_c = (\pm\delta_c, 0)$ and $\mathbf{Q}_s = (\pi/a \pm \delta_s, \pi/a)$ for the charge and spin channels, respectively. For the spin channel in Fig. 1e, the dashed line shows a fit of the lowest temperature data using two Lorentzian functions. Fig. 1c plots the charge correlations for the h -doped case along the $(Q_x, \pi/a)$ direction, where we observe a weak $(\pi/a, \pi/a)$ peak emerging at the lowest accessible temperature. This modulation is weaker than the \mathbf{Q}_c structure, such that the charge correlations are predominantly stripe-like.

We observe qualitatively different correlations in the e -doped case shown in Figs. 1b, d, and f. At high temperature ($\beta \leq 6/t$), $\chi_c(\mathbf{Q}, 0)$ has a single broad peak centered at $\mathbf{q} = (0, 0)$, which can again be decomposed into two incommensurate Lorentzian peaks centered at $\pm\delta_c$, indicative of a unidirectional charge stripe. As the temperature is lowered, these peaks sharpen and become discernible without fits while the \mathbf{q} -independent background remains constant. The charge correlations also have a relatively temperature-independent $(\pi/a, \pi/a)$ component (Fig. 1e) of similar strength as the stripe-like charge correlations. In contrast to the h -doped case, we find no indication of a spin-stripe at this doping; the spin susceptibility has a single peak centered at $(\pi/a, \pi/a)$ for all accessible temperatures.

Comparing panels a and b, we see that the charge stripe correlations in the h - and e -doped systems develop differently as the temperature decreases. In the h -doped case (Fig. 1a), the incommensurate peaks grow while δ_c shifts to smaller values as the temperature decreases [34]. In the e -doped case, the incommensurate peaks grow (Fig. 1b) while the value of $\chi_c(\mathbf{Q}, 0)$ near zone center is suppressed, resulting in well-defined peaks centered at $\approx (\pm\pi/2a, 0)$. In addition, the $(\pi/a, \pi/a)$

component is significantly stronger in the e -doped case (Fig. 1d). However, since the height of the incommensurate peaks in Fig. 1b does not appear to level off, the stripe correlations could dominate at lower temperatures.

The corresponding correlation functions in real-space, obtained at the lowest accessible temperatures ($\beta t = 6$ and 10 for the h - and e -doped cases, respectively) are plotted in Fig. 2, with the data for the h -doped case reproduced from Ref. 34. The e -doped case (Fig. 2a) has a clear short-range $(\pi/a, \pi/a)$ checkerboard-like pattern near $\mathbf{r} = 0$, superimposed over a stripe-like component. In contrast, the h -doped case (Fig. 2b) only shows a stripe pattern. Figs. 2c and d show the staggered spin correlation function. Here, the blue region in the middle represents one AFM domain, while the red region on both sides indicates neighboring AFM domains with the opposite phase (note that the staggered spin correlation function that is plotted contains an additional negative sign on the B-sublattice as explained in the Methods section). Consistent with Fig. 1 and as observed before [34], the h -doped case has a clear stripe pattern whose period is roughly twice that of the charge modulations. In contrast, the e -doped cuprates are dominated by short-range AFM correlations with only a single phase inversion appearing at longer distances. To summarize, the h -doped system has intertwined spin and charge stripe correlations, while the e -doped system manifests CDW correlation with stripe-like $\mathbf{Q} = (\delta_c, 0)$ and checkerboard $(\pi/a, \pi/a)$ components and nearly uniform AFM spin correlations.

Figure 3 examines how the stripe component of the charge correlations develops for the e -doped case with density and t' for a fixed inverse temperature $\beta = 8/t$. Fig. 3a shows $\chi_c(\mathbf{Q}, 0)$ along the $(Q_x, 0)$ direction for various densities, while holding $t'/t = -0.2$ fixed. At $\langle n \rangle = 1.125$, the charge susceptibility has a single peak

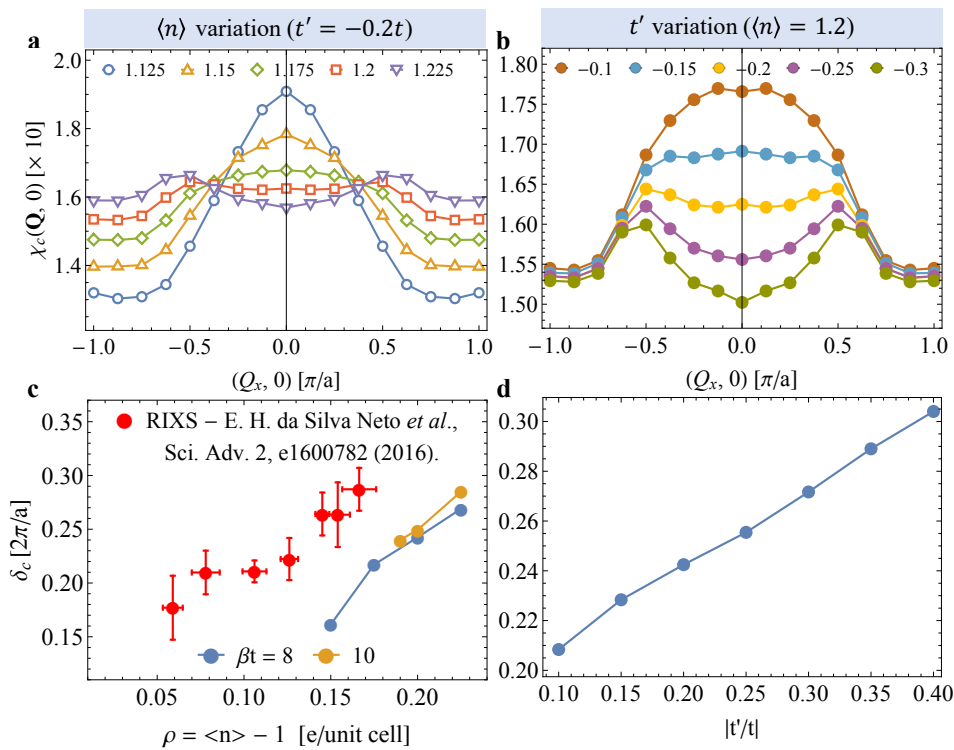


FIG. 3. **Evolution of the charge-density-wave correlations with model parameters.** **a** and **b** show $\chi_c(\mathbf{Q}, 0)$ for the e -doped case along the $(Q_x, 0)$ direction at $\beta = 8/t$. **a** shows the effect of different electron fillings $\langle n \rangle$ at $t' = -0.2t$ while **b** shows the effect of varying t' for fixed $\langle n \rangle = 1.2$. **c** The evolution of the incommensurate CDW peak $\mathbf{Q}_{\text{cdw}} = (\delta_c, 0)$ with doping, obtained from fitting the spectra in panel **a** with three Lorentzian functions and a constant background. For comparison, we also plot the measured values of \mathbf{Q}_{cdw} extracted from RIXS experiments [28]. **d** The evolution of the incommensurate CDW peak as a function of t' , obtained from fitting the data shown in panel **b**. All results were obtained on a 16×4 cluster with $U = 6t$ and $\beta t = 8$ except for the $\beta t = 10$ results in panel **c**.

centered at $\mathbf{Q} = 0$. With further electron doping, the peak splits into two well-defined peaks that become discernible without fitting for $\langle n \rangle \geq 1.2$. At the same time, the uniform background grows with doping due to the increased metallicity in the system [35]. Fig. 3b presents the same quantity for various values of t' , while fixing $\langle n \rangle = 1.2$. At $t'/t = -0.1$, the charge susceptibility again has a single broad peak at $\mathbf{Q} = 0$. As $|t'|$ increases, the middle peak is suppressed, leading to the appearance of a pair of incommensurate peaks. At the same time, the uniform background remains almost unchanged.

To assess these trends quantitatively, we fit the curves in Fig. 3a with three Lorentzian functions centered at $Q_x = 0$ and $\pm Q_c$ plus a constant background to extract the wave vector $\delta_c = Q_c/(2\pi/a)$. As shown in Fig. 3c, δ_c increases approximately linearly as a function of the doping $\rho = \langle n \rangle - 1$. This trend agrees with experimental observations for the e -doped cuprates [28]; however, the observed $\mathbf{Q}_{\text{cdw}}(\rho)$ curve is shifted to lower doping levels relative to our results. We also extracted δ_c as a function of t' , as shown in Fig. 3d, where we find that δ_c linearly shifts to larger values with $|t'|$. Extrapolating the experimental data in Fig. 3c to $\rho = 0.2$ yields $Q_{\text{cdw}} \approx 0.32$ r.l.u., which corresponds to $|t'/t| \approx 0.4$ in our model.

This value is much larger than the typical values used to model the e -doped cuprates using the single-band model.

RIXS experiments have found that the CDW in the e -doped cuprates has a significant dynamical component [25, 28, 30]. To compare with these measurements, we show in Fig. 4 the dynamical spin and charge structure functions $S(\mathbf{Q}, \omega)$ and $N(\mathbf{Q}, \omega)$ obtained using a parameter-free differential evolution analytic continuation (DEAC) algorithm [41]. (A comparison of the DEAC results to those obtained with more conventional techniques is provided in the supplement.) The dynamic spin structure factor $S(\mathbf{Q}, \omega)$ displays the typical persistent antiferromagnetic paramagnon spectrum obtained with other QMC methods [42], with large spectral weight at $\mathbf{Q} = (\pi/a, 0)$ at an energy near $\omega = t$ and a downward dispersion towards $\mathbf{Q} = 0$. The dynamic charge structure factor exhibits similar behavior with a large spectral weight near the zone edge and a downward dispersion towards the zone center. Still, the spectral weight is concentrated at higher energies.

As an approximation of the predicted RIXS intensity, Fig. 3c plots a superposition of $S(\mathbf{Q}, \omega)$ and $N(\mathbf{Q}, \omega)$. Due to the vastly different energy scales in the spin and charge correlations, one sees two distinct upward dispers-

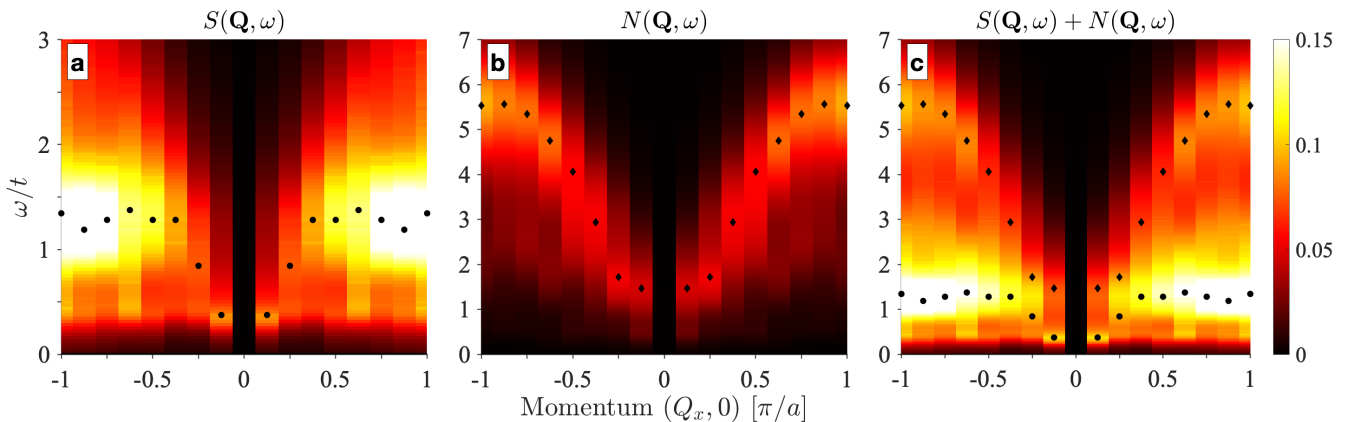


FIG. 4. **Dynamical spin and charge structure factors for the electron-doped model.** Panels **a** and **b** show the dynamical spin $S(\mathbf{Q}, \omega)$ and charge $N(\mathbf{Q}, \omega)$ structure factors, respectively, along the $\mathbf{Q} = (Q_x, 0)$ direction. Results are shown for an electron-doped model with $t'/t = 0.25$ and $n = 1.2$, obtained on a 16×4 cluster with $U = 6t$ and $\beta/t = 10$. Panel **c** shows the sum of the two as a crude approximation for Cu L -edge RIXS spectra. The black circles and diamonds indicate the locations of the maxima in $S(\mathbf{Q}, \omega)$ and $N(\mathbf{Q}, \omega)$, respectively. All panels are plotted on the same color scale, as indicated on the right.

ing branches, i.e., a low energy branch due to the spin correlations and a high energy branch due to the charge correlations. Since the spin correlations have a much larger amplitude, the low energy branch has a stronger overall intensity, while the higher energy (charge) branch is muted. The behavior for the dynamical correlations near zone center agrees well with the data reported in Ref. [30]. Our results on the higher-energy charge excitations call for future RIXS measurements in this regime; however, the high-energy portion of the charge excitations are expected to overlap with the dd -excitations [43].

Discussion. The correlations in the e -doped case cannot be attributed solely to the weak-coupling Lindhard physics [44]. For example, as discussed in the supplementary materials, if we adjust the effective U in a random-phase approximation (RPA) to match the charge correlations $\chi_c(Q_c, 0)$ then the predicted correlations at $(\pi/a, \pi/a)$ are much stronger than those reported here. Similarly, we do not resolve any peak structure in $\chi_s(\mathbf{Q}, 0)$ along the $(Q_x, 0)$ direction as one would expect in such a weak-coupling framework. While the peak positions predicted by RPA are close to the values reported here for $\langle n \rangle = 1.2$, the resulting temperature, doping, and t' evolution is inconsistent with the observed behavior (see supplement).

We have demonstrated that the CDW correlations observed in DCA simulations of the single-band Hubbard model have a pronounced particle-hole asymmetry. Our results for the e -doped system are also in qualitative agreement with RIXS experiments on $\text{Nd}_{2-x}\text{Ce}_x\text{CuO}_4$ [25, 30]; however, there are some notable quantitative differences. For example, our predicted $\delta_c(\rho)$ dependence is shifted to higher electron doping in comparison to experiment. This discrepancy may be re-

lated to challenges in determining the carrier concentration in the CuO_2 planes. ARPES measurements of $\text{Pr}_{1.3-x}\text{La}_{0.7}\text{Ce}_x\text{CuO}_{4-\delta}$ (PLCCO), for example, have suggested that the doped electron concentration of CuO_2 plane can be larger than the Ce concentration x by up to $0.08 e/\text{Cu}$, depending on the annealing method [45]. This discrepancy is comparable to the shift observed in Fig. 3c. Adjusting the value of t' could also partially account for this difference; single-band fits to the measured Fermi surface of PLCCO estimate $|t'/t| = 0.4 - 0.34$. Finally, the periodicity of the charge modulations may be affected by the DCA mean-field [34]. In the h -doped case, DCA and DQMC predict different stripe periods for the same model parameters. Nevertheless, our calculations reproduce the qualitative doping dependence observed in the real materials and support the notion that the single-band Hubbard model captures the physics of the e -doped cuprates.

Methods

The Model. We consider the single-band Hubbard model on a two-dimensional square lattice. The Hamiltonian is

$$H = - \sum_{\mathbf{i}, \mathbf{j}, \sigma} t_{\mathbf{i}, \mathbf{j}} c_{\mathbf{i}, \sigma}^\dagger c_{\mathbf{j}, \sigma} - \mu \sum_{\mathbf{i}, \sigma} n_{\mathbf{i}, \sigma} + U \sum_{\mathbf{i}} n_{\mathbf{i}, \uparrow} n_{\mathbf{i}, \downarrow}. \quad (1)$$

Here, $c_{\mathbf{i}, \sigma}^\dagger$ ($c_{\mathbf{i}, \sigma}$) creates (annihilates) a spin- σ ($=\uparrow, \downarrow$) electron at site $\mathbf{i} = a(i_x, i_y)$, where $a = 1$ is the lattice constant, $t_{\mathbf{i}, \mathbf{j}}$ is the hopping integral between sites \mathbf{i} and \mathbf{j} , μ is the chemical potential, and U is the Hubbard repulsion. To model the cuprates, we set $t_{\mathbf{i}, \mathbf{j}} = t$ and t' for nearest and next-nearest-neighbor hopping, respectively, and zero otherwise, and take $U/t = 6$ unless

stated otherwise.

The dynamical cluster approximation. We study the model in Eq. (1) using DCA [8, 39, 46] as implemented in the DCA++ code [47]. The DCA represents the infinite bulk lattice in the thermodynamic limit by a finite-size cluster embedded in a self-consistent dynamical mean-field. The intra-cluster correlations are treated exactly, while the mean field approximates the inter-cluster degrees of freedom. We use rectangular $N_c = 16 \times 4$ clusters that are large enough to support spin and charge stripe correlations if they are present in the model [34].

Assuming short-ranged correlations, the self-energy $\Sigma(\mathbf{k}, i\omega_n)$ can be approximated by the cluster self-energy $\Sigma(\mathbf{K}, i\omega_n)$, where \mathbf{K} are the cluster momenta. We obtain the coarse-grained single-particle Green function

$$\begin{aligned} \bar{G}(\mathbf{K}, i\omega_n) &= \frac{N_c}{N} \sum_{\mathbf{k}'} G(\mathbf{K} + \mathbf{k}', i\omega_n) \\ &= \frac{N_c}{N} \sum_{\mathbf{k}'} \frac{1}{i\omega_n + \mu - \varepsilon(\mathbf{K} + \mathbf{k}') - \Sigma(\mathbf{K}, i\omega_n)}, \end{aligned} \quad (2)$$

by averaging the lattice Green function $G(\mathbf{k}, i\omega_n)$ over the N/N_c momenta \mathbf{k}' in a patch about the cluster momentum \mathbf{K} . (N and N_c are the number of site in the lattice and cluster, respectively.) In this way, the bulk problem is reduced to a finite-size-cluster problem.

We solve the cluster problem with the continuous-time, auxiliary-field quantum Monte-Carlo algorithm (CT-AUX) [40, 48]. The expansion order of the CT-AUX QMC algorithm is typically 500-1500, depending on the temperature and value of t' . Depending on the value of the average fermion sign for a given parameter set, we measure $1 - 5 \times 10^8$ samples for the correlation functions. Six to eight iterations of the DCA loop are typically needed to obtain good convergence for the DCA cluster self-energy.

To study the spin and charge correlations, we measure the static ($\omega = 0$) real-space spin-spin correlation function

$$\chi_s(\mathbf{r}, 0) = \frac{1}{N} \sum_{\mathbf{i}} \int_0^\beta \langle \hat{S}_{\mathbf{r}+\mathbf{i}}^z(\tau) \hat{S}_{\mathbf{i}}^z(0) \rangle d\tau \quad (3)$$

and density-density correlation function

$$\chi_c(\mathbf{r}, 0) = \frac{1}{N} \int_0^\beta [\langle n_{\mathbf{r}+\mathbf{i}}(\tau) n_{\mathbf{i}}(0) \rangle - \langle n_{\mathbf{r}+\mathbf{i}}(\tau) \rangle \langle n_{\mathbf{i}}(0) \rangle] d\tau. \quad (4)$$

Here, $\mathbf{r} = (r_x, r_y)a$ is a lattice vector, $\hat{S}_{\mathbf{i}}^z = \frac{1}{2}(n_{\mathbf{i},\uparrow} - n_{\mathbf{i},\downarrow})$ is the z -component of the local spin operator and $n_{\mathbf{i}} = \sum_{\sigma} c_{\mathbf{i},\sigma}^\dagger c_{\mathbf{i},\sigma}$ is the local density operator. The static momentum-space susceptibilities $\chi_c(\mathbf{Q}, 0)$ and $\chi_s(\mathbf{Q}, 0)$ are obtained by a Fourier transform. We also plot the staggered spin correlation function

$\chi_{s,\text{stag}}(\mathbf{r}) = (-1)^{(r_x+r_y)} S(\mathbf{r}, 0)$ to highlight the relative phases of the antiferromagnetic domains.

Analytic continuation. The dynamical charge structure factor $N(\mathbf{Q}, \omega)$ is obtained from the imaginary part of the charge susceptibility using

$$N(\mathbf{Q}, \omega) = \frac{\text{Im}\chi_c(\mathbf{Q}, \omega)}{1 - e^{-\beta\omega}}. \quad (5)$$

(The dynamical spin structure factor $S(\mathbf{Q}, \omega)$ and spin susceptibility $\chi_s(\mathbf{Q}, \omega)$ satisfy a similar equation.)

The real frequency susceptibility is related to the imaginary time susceptibility by the integral equation

$$\chi_{s,c}(\mathbf{Q}, \tau) = \int_0^\infty \frac{d\omega}{\pi} \frac{e^{-\tau\omega} + e^{-(\beta-\tau)\omega}}{1 - e^{-\beta\omega}} \text{Im}\chi_{s,c}(\mathbf{Q}, \omega). \quad (6)$$

Inverting this relationship to obtain $\text{Im}\chi(\mathbf{Q}, \omega)$ is an ill-posed problem. We used three independent methods to perform the analytic continuation to gauge our relative confidence in the various features. These include the method of Maximum Entropy [49], a parameter-free differential evolution algorithm [41], and stochastic optimization [50]. The results obtained using the differential evolution algorithm are shown in the main text, while the remaining results are provided in the supplement.

Acknowledgements: We thank M. P. M. Dean and J. Pelliciani for their valuable discussions. This work was supported by the U.S. Department of Energy, Office of Science, Office of Basic Energy Sciences, under Award Number DE-SC0022311. This research used resources of the Oak Ridge Leadership Computing Facility, which is a DOE Office of Science User Facility supported under Contract No. DE-AC05-00OR22725.

Author Contributions: P.M. performed the DCA calculations, analyzed the data, and carried out the MaxEnt analytic continuation calculations; N.S.N. and A.D.M. developed the differential evolution analytic continuation code and performed analyses with this method; F.B. developed the stochastic optimization code and performed analyses with this method. S.K. and T.A.M. developed the DCA code. T.A.M. and S.J. supervised the project; P.M., T.A.M., and S.J. wrote the paper with input from all authors.

Code Availability: The DCA++ code used for this project can be obtained at <https://github.com/CompFUSE/DCA>. The DEAC code can be obtained at <https://github.com/DelMaestroGroup/papers-code-DEAC>. All other codes will be made available upon request.

Data Availability: The data supporting this study will be deposited in a public repository once the final version of the paper is accepted for publication. Until then, data

will be made available upon reasonable requests made to

S.J. (sjohn145@utk.edu) or T.A.M. (maier@ornl.gov).

-
- [1] D. J. Scalapino, A common thread: The pairing interaction for unconventional superconductors, *Rev. Mod. Phys.* **84**, 1383 (2012).
- [2] D. P. Arovas, E. Berg, S. A. Kivelson, and S. Raghu, The Hubbard model, *Annual Review of Condensed Matter Physics* **13**, 239 (2022).
- [3] M. Qin, T. Schäfer, S. Andergassen, P. Corboz, and E. Gull, TheHubbard model: A computational perspective, *Annual Review of Condensed Matter Physics* **13**, 275 (2022).
- [4] F. C. Zhang and T. M. Rice, Effective hamiltonian for the superconducting cu oxides, *Phys. Rev. B* **37**, 3759 (1988).
- [5] C. Batista and A. Aligia, Validity of the $t - J$ model: Quantum numbers for $(\text{Cu}_4\text{O}_8)^{-7}$, *Solid State Communications* **83**, 419 (1992).
- [6] P. Mai, G. Balduzzi, S. Johnston, and T. A. Maier, Orbital structure of the effective pairing interaction in the high-temperature superconducting cuprates, *npj Quantum Materials* **6**, 26 (2021).
- [7] S. Li, A. Nocera, U. Kumar, and S. Johnston, Particle-hole asymmetry in the dynamical spin and charge responses of corner-shared 1D cuprates, *Communications Physics* **4**, 217 (2021).
- [8] T. A. Maier, M. Jarrell, T. C. Schulthess, P. R. C. Kent, and J. B. White, Systematic study of d -wave superconductivity in the 2D repulsive Hubbard model, *Phys. Rev. Lett.* **95**, 237001 (2005).
- [9] B.-X. Zheng, C.-M. Chung, P. Corboz, G. Ehlers, M.-P. Qin, R. M. Noack, H. Shi, S. R. White, S. Zhang, and G. K.-L. Chan, Stripe order in the underdoped region of the two-dimensional Hubbard model, *Science* **358**, 1155 (2017).
- [10] E. W. Huang, C. B. Mendl, H.-C. Jiang, B. Moritz, and T. P. Devereaux, Stripe order from the perspective of the Hubbard model, *npj Quantum Materials* **3**, 22 (2018).
- [11] M. Qin, C.-M. Chung, H. Shi, E. Vitali, C. Hubig, U. Schollwöck, S. R. White, and S. Zhang (Simons Collaboration on the Many-Electron Problem), Absence of superconductivity in the pure two-dimensional Hubbard model, *Phys. Rev. X* **10**, 031016 (2020).
- [12] S. Jiang, D. J. Scalapino, and S. R. White, Ground-state phase diagram of the t - J model, *Proceedings of the National Academy of Sciences* **118**, e2109978118 (2021).
- [13] H. Xu, H. Shi, E. Vitali, M. Qin, and S. Zhang, Stripes and spin-density waves in the doped two-dimensional Hubbard model: Ground state phase diagram, *Phys. Rev. Research* **4**, 013239 (2022).
- [14] H.-C. Jiang and T. P. Devereaux, Superconductivity in the doped Hubbard model and its interplay with next-nearest hopping t' , *Science* **365**, 1424 (2019).
- [15] C.-M. Chung, M. Qin, S. Zhang, U. Schollwöck, and S. R. White (The Simons Collaboration on the Many-Electron Problem), Plaquette versus ordinary d -wave pairing in the t' -Hubbard model on a width-4 cylinder, *Phys. Rev. B* **102**, 041106 (2020).
- [16] C. C. Tsuei and J. R. Kirtley, Pairing symmetry in cuprate superconductors, *Rev. Mod. Phys.* **72**, 969 (2000).
- [17] R. Comin and A. Damascelli, Resonant x-ray scattering studies of charge order in cuprates, *Annual Review of Condensed Matter Physics* **7**, 369 (2016).
- [18] R. Arpaia and G. Ghiringhelli, Charge order at high temperature in cuprate superconductors, *Journal of the Physical Society of Japan* **90**, 111005 (2021).
- [19] J. M. Tranquada, B. J. Sternlieb, J. D. Axe, Y. Nakamura, and S. Uchida, Evidence for stripe correlations of spins and holes in copper oxide superconductors, *Nature* **375**, 561 (1995).
- [20] J. E. Hoffman, E. W. Hudson, K. M. Lang, V. Madhavan, H. Eisaki, S. Uchida, and J. C. Davis, A four unit cell periodic pattern of quasi-particle states surrounding vortex cores in $\text{Bi}_2\text{Sr}_2\text{CaCu}_2\text{O}_{8+\delta}$, *Science* **295**, 466 (2002).
- [21] T. Hanaguri, C. Lupien, Y. Kohsaka, D. H. Lee, M. Azuma, M. Takano, H. Takagi, and J. C. Davis, A ‘checkerboard’ electronic crystal state in lightly hole-doped $\text{Ca}_{2-x}\text{Na}_x\text{CuO}_2\text{Cl}_2$, *Nature* **430**, 1001 (2004).
- [22] M. d’Astuto, P. K. Mang, P. Giura, A. Shukla, P. Ghigna, A. Mirone, M. Braden, M. Greven, M. Krisch, and F. Sette, Anomalous dispersion of longitudinal optical phonons in $\text{Nd}_{1.86}\text{Ce}_{0.14}\text{CuO}_{4+\delta}$ determined by inelastic x-ray scattering, *Phys. Rev. Lett.* **88**, 167002 (2002).
- [23] M. Braden, L. Pintschovius, T. Uefuji, and K. Yamada, Dispersion of the high-energy phonon modes in $\text{Nd}_{1.85}\text{Ce}_{0.15}\text{CuO}_4$, *Phys. Rev. B* **72**, 184517 (2005).
- [24] G. Ghiringhelli, M. L. Tacon, M. Minola, S. Blanco-Canosa, C. Mazzoli, N. B. Brookes, G. M. D. Luca, A. Frano, D. G. Hawthorn, F. He, T. Loew, M. M. Sala, D. C. Peets, M. Salluzzo, E. Schierle, R. Sutarto, G. A. Sawatzky, E. Weschke, B. Keimer, and L. Braicovich, Long-range incommensurate charge fluctuations in $(\text{Y,Nd})\text{Ba}_2\text{Cu}_3\text{O}_{6+x}$, *Science* **337**, 821 (2012).
- [25] E. H. da Silva Neto, P. Aynajian, A. Frano, R. Comin, E. Schierle, E. Weschke, A. Gyenis, J. Wen, J. Schneeloch, Z. Xu, S. Ono, G. Gu, M. L. Tacon, and A. Yazdani, Ubiquitous interplay between charge ordering and high-temperature superconductivity in cuprates, *Science* **343**, 393 (2014).
- [26] R. Comin, A. Frano, M. M. Yee, Y. Yoshida, H. Eisaki, E. Schierle, E. Weschke, R. Sutarto, F. He, A. Soumyanarayanan, Y. He, M. L. Tacon, I. S. Elfimov, J. E. Hoffman, G. A. Sawatzky, B. Keimer, and A. Damascelli, Charge order driven by fermi-arc instability in $\text{Bi}_2\text{Sr}_{2-x}\text{La}_x\text{CuO}_{6+\delta}$, *Science* **343**, 390 (2014).
- [27] W. Tabis, Y. Li, M. L. Tacon, L. Braicovich, A. Kreyssig, M. Minola, G. Della, E. Weschke, M. J. Veit, M. Ramazanoglu, A. I. Goldman, T. Schmitt, G. Ghiringhelli, N. Barišić, M. K. Chan, C. J. Dorow, G. Yu, X. Zhao, B. Keimer, and M. Greven, Charge order and its connection with fermi-liquid charge transport in a pristine high- T_c cuprate, *Nature Communications* **5**, 5875 (2014).
- [28] E. H. da Silva Neto, B. Yu, M. Minola, R. Sutarto, E. Schierle, F. Boschini, M. Zonno, M. Bluschke, J. Higgins, Y. Li, G. Yu, E. Weschke, F. He, M. L. Tacon, R. L. Greene, M. Greven, G. A. Sawatzky, B. Keimer, and A. Damascelli, Doping-dependent charge order cor-

- relations in electron-doped cuprates, *Science Advances* **2**, e1600782 (2016).
- [29] H. Jang, S. Asano, M. Fujita, M. Hashimoto, D. H. Lu, C. A. Burns, C.-C. Kao, and J.-S. Lee, Superconductivity-insensitive order at $q \sim 1/4$ in electron-doped cuprates, *Phys. Rev. X* **7**, 041066 (2017).
- [30] E. H. da Silva Neto, M. Minola, B. Yu, W. Tabis, M. Bluschke, D. Unruh, H. Suzuki, Y. Li, G. Yu, D. Betto, K. Kummer, F. Yakhov, N. B. Brookes, M. Le Tacon, M. Greven, B. Keimer, and A. Damascelli, Coupling between dynamic magnetic and charge-order correlations in the cuprate superconductor $\text{Nd}_{2-x}\text{Ce}_x\text{CuO}_4$, *Phys. Rev. B* **98**, 161114 (2018).
- [31] Y. Y. Peng, R. Fumagalli, Y. Ding, M. Minola, S. Caprara, D. Betto, M. Bluschke, G. M. De Luca, K. Kummer, E. Lefrançois, M. Salluzzo, H. Suzuki, M. Le Tacon, X. J. Zhou, N. B. Brookes, B. Keimer, L. Braicovich, M. Grilli, and G. Ghiringhelli, Re-entrant charge order in overdoped $(\text{Bi,Pb})_{2.12}\text{Sr}_{1.88}\text{CuO}_{6+\delta}$ outside the pseudogap regime, *Nature Materials* **17**, 697 (2018).
- [32] H. Miao, R. Fumagalli, M. Rossi, J. Lorenzana, G. Seibold, F. Yakhov-Harris, K. Kummer, N. B. Brookes, G. D. Gu, L. Braicovich, G. Ghiringhelli, and M. P. M. Dean, Formation of incommensurate charge density waves in cuprates, *Phys. Rev. X* **9**, 031042 (2019).
- [33] H. Y. Huang, A. Singh, C. Y. Mou, S. Johnston, A. F. Kemper, J. van den Brink, P. J. Chen, T. K. Lee, J. Okamoto, Y. Y. Chu, J. H. Li, S. Komiya, A. C. Komarek, A. Fujimori, C. T. Chen, and D. J. Huang, Quantum fluctuations of charge order induce phonon softening in a superconducting cuprate, *Phys. Rev. X* **11**, 041038 (2021).
- [34] P. Mai, S. Karakuzu, G. Balduzzi, S. Johnston, and T. A. Maier, Intertwined spin, charge, and pair correlations in the two-dimensional Hubbard model in the thermodynamic limit, *Proceedings of the National Academy of Sciences* **119**, e2112806119 (2022).
- [35] E. W. Huang, T. Liu, W. O. Wang, H.-C. Jiang, P. Mai, T. A. Maier, S. Johnston, B. Moritz, and T. P. Devereaux, Fluctuating intertwined stripes in the strange metal regime of the Hubbard model, *arXiv:2202.08845* (2022).
- [36] S. Sorella, The phase diagram of the Hubbard model by variational auxiliary field quantum Monte Carlo, *arXiv:2101.07045* (2021).
- [37] A. Wietek, Y.-Y. He, S. R. White, A. Georges, and E. M. Stoudenmire, Stripes, antiferromagnetism, and the pseudogap in the doped Hubbard model at finite temperature, *Phys. Rev. X* **11**, 031007 (2021).
- [38] B. Xiao, Y.-Y. He, A. Georges, and S. Zhang, Temperature dependence of spin and charge orders in the doped two-dimensional Hubbard model, *arXiv:2202.11741* (2022).
- [39] T. Maier, M. Jarrell, T. Pruschke, and M. H. Hettler, Quantum cluster theories, *Rev. Mod. Phys.* **77**, 1027 (2005).
- [40] E. Gull, P. Werner, O. Parcollet, and M. Troyer, Continuous-time auxiliary-field Monte Carlo for quantum impurity models, *EPL (Europhysics Letters)* **82**, 57003 (2008).
- [41] N. S. Nichols, P. Sokol, and A. Del Maestro, Parameter-free differential evolution algorithm for the analytic continuation of imaginary time correlation functions, *Phys. Rev. E* **106**, 025312 (2022).
- [42] C. J. Jia, E. A. Nowadnick, K. Wohlfeld, Y. F. Kung, C. C. Chen, S. Johnston, T. Tohyama, B. Moritz, and T. P. Devereaux, Persistent spin excitations in doped antiferromagnets revealed by resonant inelastic light scattering, *Nature Communications* **5**, 3314 (2014).
- [43] K. Ishii, M. Fujita, T. Sasaki, M. Minola, G. Dellea, C. Mazzoli, K. Kummer, G. Ghiringhelli, L. Braicovich, T. Tohyama, K. Tsutsumi, K. Sato, R. Kajimoto, K. Ikeuchi, K. Yamada, M. Yoshida, M. Kurooka, and J. Mizuki, High-energy spin and charge excitations in electron-doped copper oxide superconductors, *Nature Communications* **5**, 3714 (2014).
- [44] F. Šimkovic, R. Rossi, and M. Ferrero, The weak, the strong and the long correlation regimes of the two-dimensional Hubbard model at finite temperature, *arXiv:2110.05863* (2021).
- [45] C. Lin, T. Adachi, M. Horio, T. Ohgi, M. A. Baqiya, T. Kawamata, H. Sato, T. Sumura, K. Koshiishi, S. Nakata, G. Shibata, K. Hagiwara, M. Suzuki, K. Ono, K. Horiba, H. Kumigashira, S. Ideta, K. Tanaka, Y. Koike, and A. Fujimori, Extended superconducting dome revealed by angle-resolved photoemission spectroscopy of electron-doped cuprates prepared by the protect annealing method, *Phys. Rev. Research* **3**, 013180 (2021).
- [46] M. Jarrell, T. Maier, C. Huscroft, and S. Moukouri, Quantum Monte Carlo algorithm for nonlocal corrections to the dynamical mean-field approximation, *Phys. Rev. B* **64**, 195130 (2001).
- [47] U. R. Hähner, G. Alvarez, T. A. Maier, R. Solcà, P. Staar, M. S. Summers, and T. C. Schulthess, DCA++: A software framework to solve correlated electron problems with modern quantum cluster methods, *Commun. Phys.* **246**, 106709 (2020).
- [48] E. Gull, P. Staar, S. Fuchs, P. Nukala, M. Summers, T. Pruschke, T. Schulthess, and T. Maier, Submatrix updates for the continuous-time auxiliary-field algorithm, *Physical Review B* **83**, 75122 (2011).
- [49] M. Jarrell and J. Gubernatis, Bayesian inference and the analytic continuation of imaginary-time quantum Monte Carlo data, *Physics Reports* **269**, 133 (1996).
- [50] F. Bao, Y. Tang, M. Summers, G. Zhang, C. Webster, V. Scarola, and T. A. Maier, Fast and efficient stochastic optimization for analytic continuation, *Phys. Rev. B* **94**, 125149 (2016).
- [51] U. R. Hähner, T. A. Maier, and T. C. Schulthess, Continuous momentum dependence in the dynamical cluster approximation, *Physical Review B* **101**, 195114 (2020).
- [52] T. A. Maier, M. Jarrell, and D. J. Scalapino, Spin susceptibility representation of the pairing interaction for the two-dimensional Hubbard model, *Physical Review B* **75**, 134519 (2007).
- [53] T. A. Maier, A. Macridin, M. Jarrell, and D. J. Scalapino, Systematic analysis of a spin-susceptibility representation of the pairing interaction in the two-dimensional Hubbard model, *Physical Review B* **76**, 144516 (2007), publisher: American Physical Society.

Supplementary Information for “Robust charge-density wave correlations in the electron-doped single-band Hubbard model”

Supplementary Note 1. Comparisons of the full static charge susceptibility to weak coupling pictures

In this section, we compare the interacting static charge susceptibility for the electron-doped model (see Figs. 1 and 3 of the main text) to the static charge susceptibility computed using the bare and interacting Green’s functions (without and with random phase approximation (RPA)).

In the non-interacting limit, the charge susceptibility is given by the Lindhard formula

$$\chi_{c,G_0G_0}(\mathbf{Q}, 0) = \frac{1}{N_{\text{sites}}} \sum_{\mathbf{k}} \frac{f(\varepsilon_{\mathbf{k}}) - f(\varepsilon_{\mathbf{k}+\mathbf{Q}})}{\varepsilon_{\mathbf{k}+\mathbf{Q}} - \varepsilon_{\mathbf{k}} + i\delta}, \quad (\text{S1})$$

where $f(x) = 1/[e^{\beta(x-\mu)} + 1]$ is the Fermi-Dirac distribution function with the appropriate chemical potential μ for the targeted density n . The calculation for Eq. (S1) is performed on an $N_{\text{sites}} = 160 \times 40$ cluster to eliminate finite-size effects. In the interacting case, the charge susceptibility in Eq. (4) can be calculated using the single-particle Green’s function within the bubble approximation and discarding the vertex corrections

$$\chi_{c,GG}(\mathbf{Q}, 0) = \frac{1}{\beta N_{\text{sites}}} \sum_{\omega_n, \mathbf{k}} G(\mathbf{k}, i\omega_n) G(\mathbf{k} + \mathbf{Q}, i\omega_n). \quad (\text{S2})$$

To compare the Lindhard result better and reduce the finite-size effects, we calculated $\chi_{c,GG}$ using the lattice Green function by interpolating the DCA cluster self-energy onto a 160×40 lattice [51]. With $\chi_{c,GG}$, we calculate the corresponding RPA susceptibility

$$\chi_{c,\text{RPA}}(\mathbf{Q}, 0) = \frac{\chi_{c,GG}(\mathbf{Q}, 0)}{1 + U_{\text{eff}} \chi_{c,GG}(\mathbf{Q}, 0)} \quad (\text{S3})$$

with an effective coupling strength U_{eff} that is reduced from the bare U due to screening effects [52, 53].

The results of $\chi_{c,GG}$, χ_{c,G_0G_0} and $\chi_{c,\text{RPA}}$ in the static limit ($\omega = 0$) are compared to the full static charge susceptibility χ_c obtained from DCA in Figs. S1-S3. Specifically, we show results for varying temperature (Fig. S1), density (Fig. S2), and next-nearest-neighbor hopping (Fig. S3) along the $(Q_x, 0)$ and $(Q_x, \pi/a)$ directions, respectively.

Our first observation in Figs. S1-S3 is that generally $\chi_{c,GG}$ is similar to χ_{c,G_0G_0} in line shape with a smaller (by 20%) magnitude. χ_{c,G_0G_0} and $\chi_{c,GG}$ both show a dominant peak at $(\pi/a, \pi/a)$, and a strongly suppressed double-peak

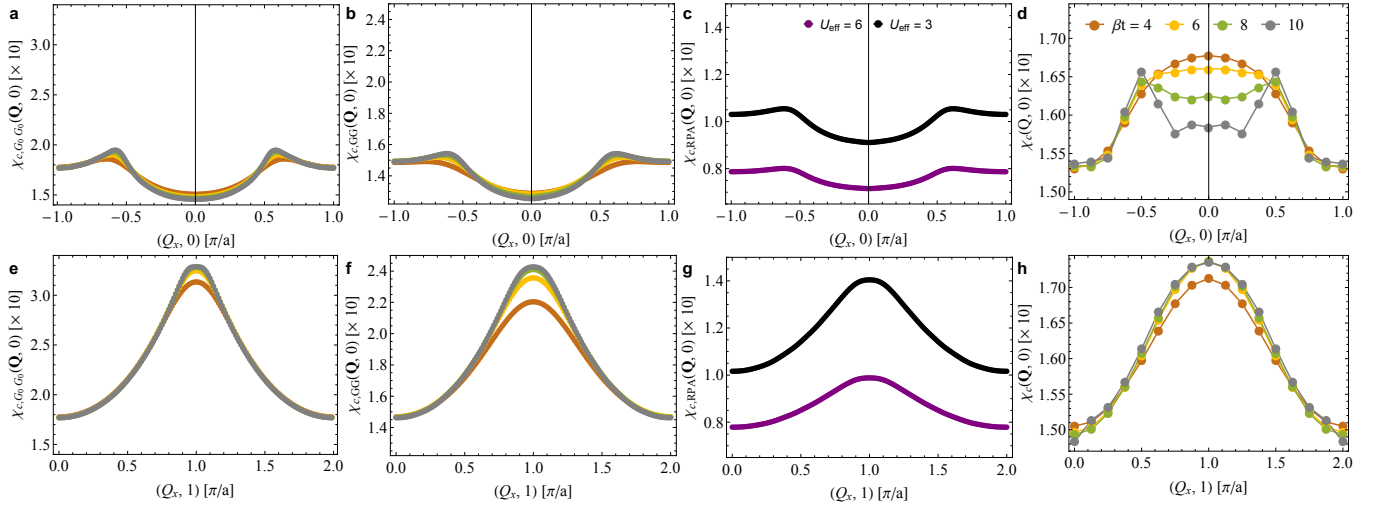


FIG. S1. The static charge susceptibility from the Lindhard function at $U/t = 0$ [panels a, e] and bubble approximation at $U/t = 6$ [panels b, f] with varying temperature. Panels c & g show the RPA result at the lowest temperature with two different U_{eff} . Panels d & h are a copy of Fig. 1d & e in the main text. The first row is for fixed $Q_y = 0$, and the second row is along $Q_y = \pi/a$. All panels except c and g share the same legend. The filling and next-nearest-neighbor hopping are $\langle n \rangle = 1.2$ and $t' = -0.2t$ for all panels.

structure along the $(Q_x, 0)$ direction. These line shapes are in huge contrast to χ_c from the numerically exact DCA calculation. In the DCA results for χ_c (far right panels **d** and **h** of Figs. S1-S3), the double peaks at fixed $Q_y = 0$ are comparable in magnitude to the $(\pi/a, \pi/a)$ peak, which is significantly weaker than $\chi_{c,GG}$ (panels **b** and **f** of Figs. S1-S3). The RPA corrected results in panels **c** and **g** of Figs. S1-S3 are closer in magnitude to the DCA χ_c . However, the magnitude of the $(\pi/a, \pi/a)$ peak is still much larger than that of the double peaks along $(Q_x, 0)$. Thus, none of the weak coupling approximations, χ_{c,G_0G_0} , $\chi_{c,GG}$ and $\chi_{c,RPA}$, captures the qualitative line shape of χ_c . They also fail to characterize the evolution from a single peak at high temperatures to the the double peak structure (along $(Q_x, 0)$) at lower temperatures (Fig. S1). The same applies to the evolution with increasing carrier concentration (Fig. S2) or decreasing t' (Fig. S3).

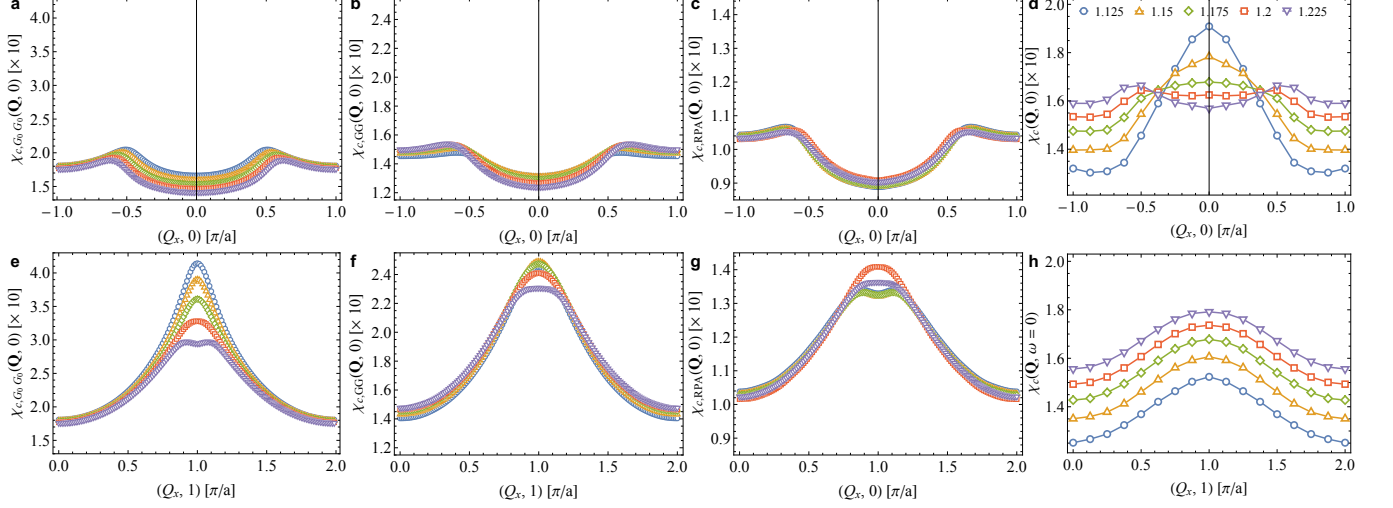


FIG. S2. The static charge susceptibility from the Lindhard function at $U = 0$ [panels **a**, **e**], bubble approximation at $U = 6$ [panels **b**, **f**] and RPA at $U_{\text{eff}} = 3$ [panels **c**, **g**] with varying density. The first row is for fixed $Q_y = 0$, and the second row is along $Q_y = \pi/a$ accordingly. Panel **d** is a copy of Fig. 3a in the main text while panel **h** shows the corresponding $\chi_c(\mathbf{Q}, 0)$ data along the (Q_x, π) direction. All panels share the same legend and are for fixed $\beta t = 8$, $t'/t = -0.2$.

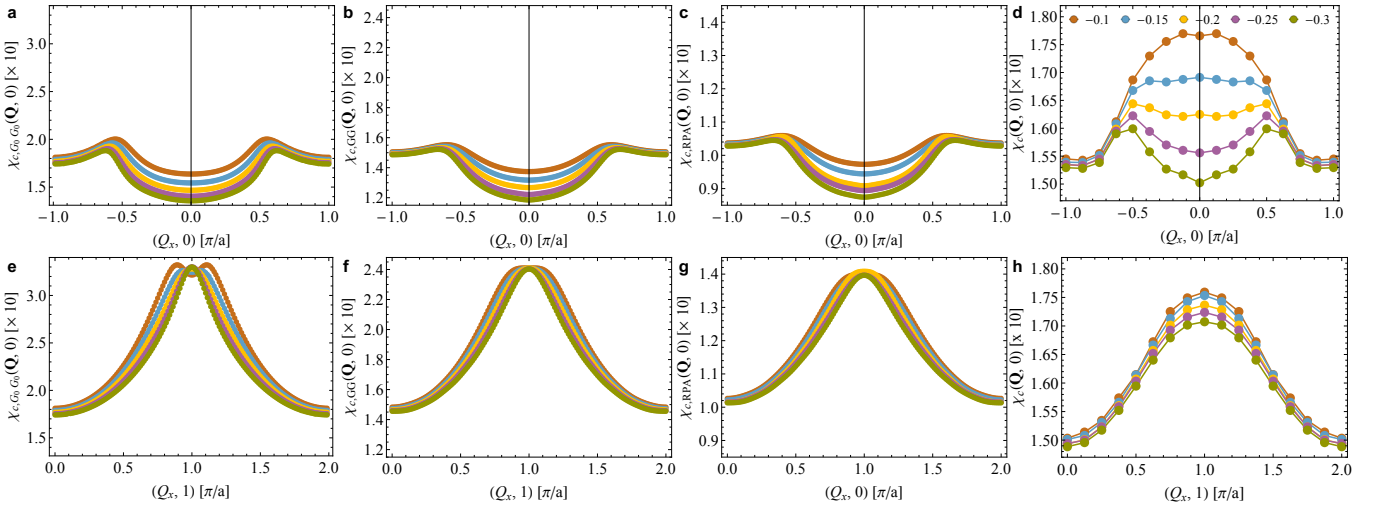


FIG. S3. The static charge susceptibility from the Lindhard function at $U = 0$ [panels **a**, **e**], bubble approximation at $U = 6$ [panels **b**, **f**] and RPA at $U_{\text{eff}} = 3$ [panels **c**, **g**] with varying t' . The first row is for fixed $Q_y = 0$, and the second row is along $Q_y = \pi/a$. Panel **d** is a copy of Fig. 3a in the main text while panel **h** shows the corresponding $\chi_c(\mathbf{Q}, 0)$ data along the (Q_x, π) direction. All panels share the same legend and are for fixed $\beta t = 8$, $\langle n \rangle = 1.2$.

In short, we find that both χ_{c,G_0G_0} , $\chi_{c,GG}$ and $\chi_{c,RPA}$ do not fully describe the qualitative features in the DCA results for χ_c . Specifically, these features include similar magnitude of the incommensurate peaks and the peak at

$(\pi/a, \pi/a)$, the evolution of the double peak structure with decreasing temperature, as well as the appearance of a central peak with $Q_y = 0$ at smaller doping density and $|t'|$. This indicates that the physics of the CDW correlations in the e -doped Hubbard model is beyond that captured in weak coupling.

Supplementary Note 2. Analytic Continuation

We used three independent methods to perform the analytic continuation of the dynamical spin $[S(\mathbf{Q}, \omega)]$ and charge $[N(\mathbf{Q}, \omega)]$ structure factors. Specifically, we used a parameter-free differential evolution algorithm [41], the method of Maximum Entropy [49], and stochastic optimization [50]. Fig. S4 compares the results obtained from these three methods. Here, $S(\mathbf{Q}, \omega)$ is shown in the first column, $N(\mathbf{Q}, \omega)$ is shown in the second column, and the sum of columns one and two is shown in the third column for reference. Results obtained using the evolution algorithm are shown in Figs. S4a-c. Similarly, results for the maximum entropy method are shown in Figs. S4d-f, and results for the stochastic optimization method are shown in Figs. S4g-i. Note that the first row is identical to the results shown in Fig. 4 of the main text.

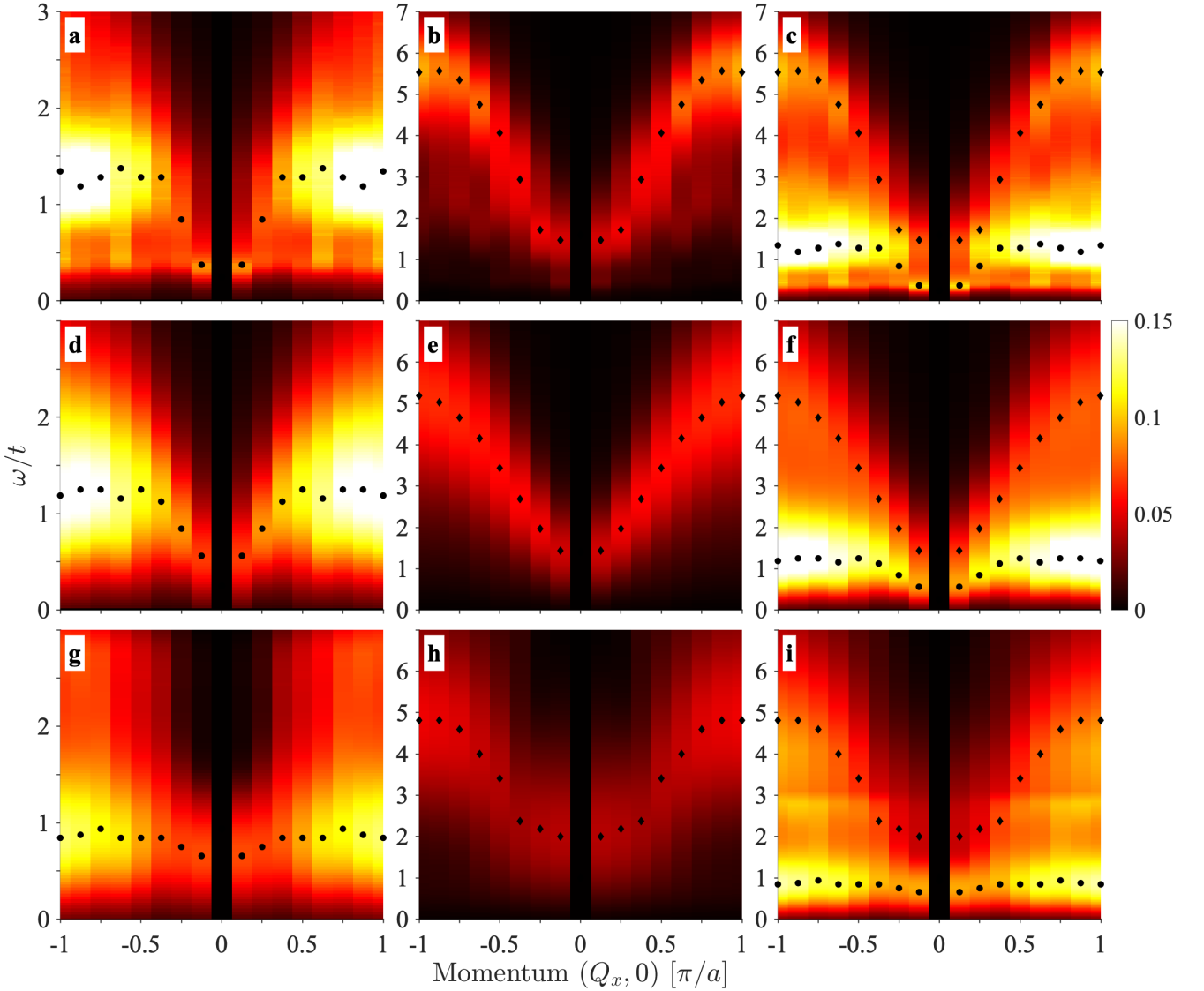


FIG. S4. A comparison of the dynamical spin $S(\mathbf{Q}, \omega)$ (left column) and charge $N(\mathbf{Q}, \omega)$ structure factors (middle column) and their sum $S(\mathbf{Q}, \omega) + N(\mathbf{Q}, \omega)$ (right column), obtained through analytic continuation using a differential evolution algorithm (top row), Maximum Entropy (middle row) and stochastic optimization (bottom row). All panels are plotted on the same color scale, as indicated on the right.